Tripartite entanglement generation in atom-coupled dual microresonator system

Abhishek Mandal [1,*] Joy Ghosh [2] Maruthi Manoj Brundavanam,[1] and Shailendra K. Varshney[3]
[1]*Department of Physics, IIT Kharagpur, Kharagpur 721302, West Bengal, India*
[2]*School of Nanoscience and Technology, IIT Kharagpur, Kharagpur 721302, West Bengal, India*
[3]*Department of Electronics and Electrical Communication Engineering, IIT Kharagpur, Kharagpur 721302, West Bengal, India*

(Received 21 November 2025; accepted 13 May 2026; published 26 May 2026)

Hybrid light-matter systems provide a powerful route to distributing quantum correlations across scalable architectures. Here, we investigate tripartite entanglement in a driven-dissipative system composed of two evanescently coupled optical resonators, one of which interacts with a two-level atom by Jaynes-Cummings-type interaction. In the weak-excitation regime, we derive an analytical steady-state description that captures how a single excitation becomes coherently shared among the three subsystems. By evaluating bipartite concurrences and the concurrence-fill measure, we identify parametric regimes where genuine tripartite entanglement between photon-atom-photon emerges despite photon loss and atomic decay. We further demonstrate how this entanglement can be controlled through experimentally accessible parameters, including detuning, light-matter coupling, photon tunneling, and coherent drive strength. The analytical predictions are fully supported by master-equation simulations, establishing a practical framework for engineering continuous-wave multipartite entanglement and enabling entanglement-assisted routing in hybrid photonic-atom quantum networks.

DOI: 10.1103/tssz-6mdr

I. INTRODUCTION

Entanglement [1,2] is a fundamental resource in modern quantum information science, enabling key advances in quantum communication [3], quantum computation [4], precision metrology [5], and related technologies. While bipartite entanglement has been extensively studied and can now be routinely generated across various physical platforms, the investigation of multipartite entanglement has opened qualitatively new directions for scaling quantum technologies [6,7].

Tripartite entanglement represents the simplest form of genuine multipartite correlations and plays a crucial role in several quantum information tasks, including quantum state sharing [8], distributed error correction [9], and network-based protocols [10], where information processing is performed across multiple nodes simultaneously. Such correlations enable cooperative distribution and processing of quantum information within a network, providing operational advantages that cannot be achieved using pairwise entanglement alone. Experimentally, multipartite entanglement

*Contact author: mandalabhi350@kgpian.iitkgp.ac.in

Published by the American Physical Society under the terms of the Creative Commons Attribution 4.0 International license. Further distribution of this work must maintain attribution to the author(s) and the published article's title, journal citation, and DOI.

has been realized in a wide range of physical systems, including cold atomic ensembles [11], optical photonic platforms [12], and superconducting quantum circuits [13].

To characterize tripartite quantum states, several entanglement measures have been developed, including the three-tangle [14], global entanglement measures [15], geometric entanglement [16], and, more recently, the concurrence fill [17]. These measures classify genuine tripartite correlations in both pure and mixed states. Although hybrid cavity-QED systems [18,19] provide promising platforms for the robust generation and control of multipartite entanglement, understanding how these entanglement measures can effectively quantify large-scale quantum correlations in physically realizable models remains largely unexplored [20].

In coupled quantum systems consisting of two-level atoms and resonators [21–25], a single excitation can be coherently shared among multiple subsystems, forming superpositions of different excitation configurations. Such delocalized single-excitation states provide a natural platform for generating multipartite quantum correlations. In particular, a single excitation can be engineered by weakly driving a photonic molecule [26,27], where the weak pumping regime restricts the system dynamics predominantly to the single-excitation manifold. When this excitation is simultaneously coupled to a two-level system, the combined atom-resonator structure forms a physically realizable tripartite platform and emerging W-type states. Although the Hilbert space in this configuration is constrained to the single-excitation manifold distributed among several parties, the generation and persistence of tripartite entanglement in any dissipative quantum system remain intriguing problems. Moreover, this minimal model provides a useful starting point that can be extended to larger multipartite architectures, enabling the exploration of entanglement distribution in open quantum networks and the generation of high-dimensional states.

This work investigates a driven-dissipative system composed of two evanescently coupled optical modes interacting with a two-level atom. We focus on the weak-excitation regime, where the dynamics are restricted to a single quantum of excitation shared among the three subsystems. In this analytically tractable limit, we derive a complete steady-state solution that reveals how coherent coupling, tunneling rate, and pumping strength collectively shape the distribution of quantum correlations. We first evaluate how bipartite concurrences are distributed among the three possible two-party partitions. We then apply the concurrence-fill measure, which identifies situations in which these correlations cannot be explained by any mixture of bipartite entanglement and must instead arise from a genuine tripartite state. To further validate this characterization, we also compute additional entanglement quantifiers. Combining analytical insights with numerical analysis, we uncover tunable regimes where the system supports steady-state tripartite entanglement even in the presence of atomic decoherence and cavity loss. Finally, we examine how these correlations can be enhanced or redistributed by tuning experimentally accessible parameters such as detuning, atom-cavity coupling, photon-hopping strength, and drive amplitude.

II. HAMILTONIAN DESCRIPTION

We consider a hybrid quantum system composed of two evanescently coupled optical microresonators and a two-level atom positioned in the near field of one of the resonators, so that the atom interacts with the resonator's evanescent field. The atom is directly coupled to the first resonator, while both resonators are coherently driven by external pump fields. The overall system dynamics are governed by a Hamiltonian incorporating photon hopping between the resonators, a Jaynes-Cummings-type atom-resonator interaction with coupling strength g, and coherent driving terms $\Omega_{1,2}$.

In a realistic experimental implementation [28], the two-level atom can be realized by several physical systems that effectively behave as artificial or natural two-level emitters. Suitable candidates include alkali atoms such as ^{87}Rb or ^{133}Cs, where the optical transitions (e.g., the D_2 line at 780 nm for ^{87}Rb) are perfectly aligned to high-Q silica or silicon nitride microresonator modes [29]. Alternatively, semiconductor quantum dots embedded in microdisk or microsphere resonators, or color centers such as nitrogen-vacancy centers in diamond coupled to whispering-gallery modes, can

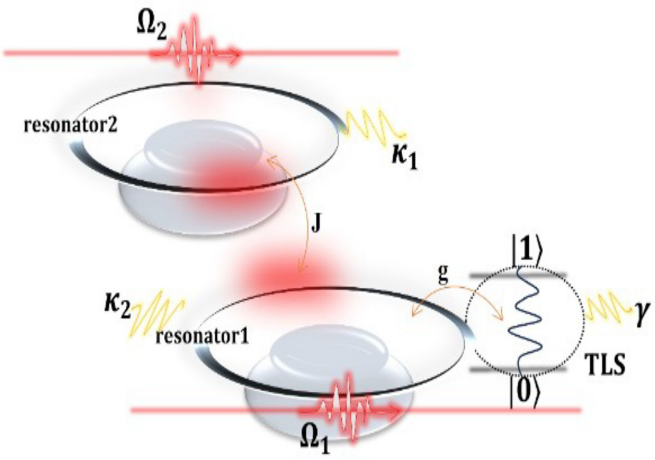


FIG. 1. Schematic diagram of the proposed model to generate tripartite entanglement. Two evanescently coupled optical resonators form a photonic molecule, where one cavity is coherently driven by a weak external field and the other interacts with a two-level atom with coupling strength g. Photons can tunnel between the cavities with a hopping rate J, while the cavities and the atom undergo dissipation characterized by decay rates κ and γ, respectively.

serve as effective two-level systems with controllable coupling strengths [30]. The photon-hopping rate J between the resonators is determined by their separation and the evanescent overlap. The complete Hamiltonian of the system is given by (taking $\hbar = 1$)

$$\hat{H} = \omega_1 \hat{a}_1^\dagger \hat{a}_1 + \omega_2 \hat{a}_2^\dagger \hat{a}_2 + \frac{\omega_a}{2}\sigma_z + J(\hat{a}_1^\dagger \hat{a}_2 + \hat{a}_2^\dagger \hat{a}_1) + g(\hat{a}_1^\dagger \sigma_- + \hat{a}_1 \sigma_+) + \Omega_1(\hat{a}_1^\dagger e^{-i\omega_L t} + \hat{a}_1 e^{i\omega_L t}) + \Omega_2(\hat{a}_2^\dagger e^{-i\omega_L t} + \hat{a}_2 e^{i\omega_L t}), \quad (1)$$

where $\omega_{1,2}$ are the frequency of resonator 1 and resonator 2, respectively, and ω_a is the atomic transition frequency. $\hat{a}(\hat{a}^\dagger)$ is the bosonic annihilation (creation) operator. $\sigma_\pm$ is the ladder operator associated with a two-level atom. σ_z is the Pauli matrix. ω_L is the laser driving frequency. g is the atom-resonator coupling strength, where J is the resonator-resonator coupling strength. $\Omega_{1,2}$ are the coherent driving amplitude of resonator 1 and resonator 2, respectively. The schematic of our proposed model is shown in Fig. 1.

To eliminate the time dependence, we consider a rotating reference frame at the laser frequency ω_L. This is achieved by applying the unitary transformation $U = \exp[i\omega_L t(\hat{a}_1^\dagger \hat{a}_1 + \hat{a}_2^\dagger \hat{a}_2 + \frac{\sigma_z}{2})]$. This transformation renders the Hamiltonian time independent, which is essential for steady-state and spectral analysis. Under this operation, the transformed Hamiltonian is given by $\hat{H}' = U\hat{H}U^\dagger - iU\frac{dU^\dagger}{dt}$. From this transformation, we introduce the detuning parameters between each resonator mode and the driving laser, defined as $\Delta_{1,2} = \omega_{1,2} - \omega_L$. Accordingly, the Hamiltonian in the rotating frame can be rewritten as

$$\hat{H}' = \Delta_1 \hat{a}_1^\dagger \hat{a}_1 + \Delta_2 \hat{a}_2^\dagger \hat{a}_2 + \frac{\Delta_a}{2}\sigma_z + J(\hat{a}_1^\dagger \hat{a}_2 + \hat{a}_2^\dagger \hat{a}_1) + g(\hat{a}_1^\dagger \sigma_- + \hat{a}_1 \sigma_+) + \Omega_1(\hat{a}_1^\dagger + \hat{a}_1) + \Omega_2(\hat{a}_2^\dagger + \hat{a}_2). \quad (2)$$

The dynamics of the hybrid resonator-atom-resonator system, as described by Eq. (2), are governed by the Lindblad master equation, which captures both coherent and dissipative processes. It can be expressed as

$$\frac{d\rho}{dt} = -i[\hat{\mathcal{H}}, \rho] + \kappa_1 \mathcal{D}[\hat{a}_1]\rho + \kappa_2 \mathcal{D}[\hat{a}_2]\rho + \gamma \mathcal{D}[\hat{\sigma}_-]\rho, \quad (3)$$

where ρ is the density matrix of the total system and $\mathcal{D}[O]\rho$ is the Lindblad super operator defined as $\mathcal{D}[O]\rho = O\rho O^\dagger - \frac{1}{2}(O^\dagger O\rho + \rho O^\dagger O)$, for a collapse operator $O \in \{\hat{a}_1, \hat{a}_2, \hat{\sigma}_-\}$. The dissipation terms $\kappa_{1,2}$ represent photon loss rates in the two resonators, while γ denotes the spontaneous decay rate of the atom. These terms are included in the Lindblad form to account for both cavity photon leakage and atomic relaxation processes. The master equation (3) is typically solved numerically using solvers such as *mesolve* using Qutip [31], which evolve $\rho(t)$ under both coherent (Hamiltonian) and incoherent (dissipative) dynamics.

For simplicity, we consider equal optical decay rates for both resonators, $\kappa_1 = \kappa_2 = \kappa$, while the atomic decay rate is denoted by γ. The corresponding non-Hermitian effective Hamiltonian can then be written as

$$\hat{H}_{\text{eff}} = \hat{H} - \frac{i\kappa}{2}(\hat{a}_1^\dagger \hat{a}_1 + \hat{a}_2^\dagger \hat{a}_2) - \frac{i\gamma}{2}\,\hat{\sigma}_+\hat{\sigma}_-. \tag{4}$$

After incorporating these dissipative terms, the full effective Hamiltonian in the rotating frame becomes

$$\begin{aligned}\hat{H}_{\text{eff}} = &\left(\Delta_1 - \frac{i\kappa}{2}\right)\hat{a}_1^\dagger \hat{a}_1 + \left(\Delta_2 - \frac{i\kappa}{2}\right)\hat{a}_2^\dagger \hat{a}_2 + \left(\frac{\Delta_a}{2} - \frac{i\gamma}{2}\right)\hat{\sigma}_z + J(\hat{a}_1^\dagger \hat{a}_2 + \hat{a}_2^\dagger \hat{a}_1) \\ &+ g(\hat{a}_1^\dagger \hat{\sigma}_- + \hat{a}_1 \hat{\sigma}_+) + \Omega_1(\hat{a}_1^\dagger + \hat{a}_1) + \Omega_2(\hat{a}_2^\dagger + \hat{a}_2).\end{aligned} \tag{5}$$

III. ENTANGLEMENT FORMULATION: BIPARTITE AND TRIPARTITE

Formally, entangled particles share a joint quantum state, represented by a nonseparable wave function, where measurements on one particle instantly determine the corresponding properties of the other(s) [1]. For bipartite systems, several robust measures exist to characterize quantum correlations, including the von Neumann entropy of the reduced density matrix for pure states [32], the concurrence and entanglement of formation for mixed two-qubit systems [33,34], and the negativity or logarithmic negativity, which are based on the Peres-Horodecki partial transpose criterion [35–37]. These measures effectively capture entanglement between two systems, as they quantify nonclassical correlations that cannot be simulated by local operations and classical communication [38].

The more challenging scenario is the quantification of entanglement in multipartite systems. In this context, the concurrence fill (F_{123}) [39] serves as a measure of genuine tripartite entanglement, which is evaluated from the reduced density matrices corresponding to different bipartitions of the full system. For each bipartite partition, the concurrence is computed using the well-known Wootters formula [33]

$$\mathcal{C}(\rho) = \max(0, \lambda_1 - \lambda_2 - \lambda_3 - \lambda_4), \tag{6}$$

where $\{\lambda_j\}$ are the square roots of the eigenvalues, arranged in decreasing order, of the non-Hermitian matrix $\rho(\sigma_y \otimes \sigma_y)\rho^*(\sigma_y \otimes \sigma_y)$. This formulation is valid when the reduced density matrices effectively correspond to two-level subsystems, which is ensured by truncating each resonator's Hilbert space to the lowest two Fock states.

To quantify genuine tripartite entanglement, Xie and Eberly [40] proposed a geometric measure based on the entanglement polygon inequality, which governs the distribution of bipartite entanglement across three subsystems. This is expressed as

$$\mathcal{C}^2_{i(jk)} \leqslant \mathcal{C}^2_{j(ki)} + \mathcal{C}^2_{k(ij)}, \tag{7}$$

where $\mathcal{C}_{i(jk)}$ represents the bipartite concurrence between the subsystem i and the combined subsystem of j and k. The concurrence fill, a measure of genuine tripartite entanglement, quantifies correlations beyond pairwise entanglement and is visualized as the area of a concurrence triangle.

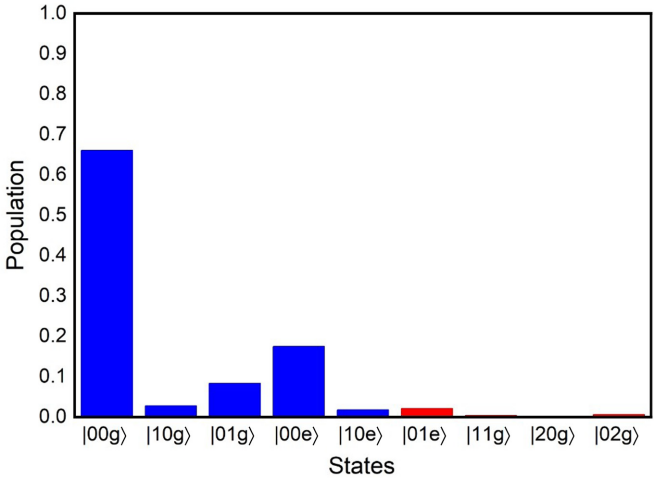


FIG. 2. Population of Fock states under weak driving condition. The blue bars denote the state population with higher probability, whereas the red bars represent the state population with extremely low probability.

It is defined as [40]

$$\mathcal{F}_{123} \equiv \left[\frac{16}{3}\left(Q-\mathcal{C}^2_{1(23)}\right)\left(Q-\mathcal{C}^2_{2(13)}\right)\left(Q-\mathcal{C}^2_{3(12)}\right)Q\right]^{1/4}, \tag{8}$$

where $Q=\frac{1}{2}(\mathcal{C}^2_{1(23)}+\mathcal{C}^2_{2(13)}+\mathcal{C}^2_{3(12)})$ ensures entanglement across all pairwise subsystems. The mathematical identity, nonzero F_{123} confirms the presence of genuine tripartite entanglement, excluding biseparability and verifying inseparability across all bipartitions.

Resonator-atom-resonator tripartite model

The tripartite concurrence structure is formed by two resonators and an atom, creating a triangle whose vertices represent the subsystems: resonator 1, an atom, and resonator 2. Each edge of the triangle corresponds to the squared concurrence between one subsystem and the composite of the remaining two. The ansatz quantum state for the model can be written as

$$\begin{aligned}|\psi\rangle = {} & c_0|00g\rangle + c_1|10g\rangle + c_2|01g\rangle + c_3|00e\rangle + c_4|10e\rangle \\ & + c_5|01e\rangle + c_6|11g\rangle + c_7|20g\rangle + c_8|02g\rangle,\end{aligned} \tag{9}$$

where g and e represent the ground and excited states of the atom, respectively. Under weak driving conditions, the population of different quantum states is shown in Fig. 2. The bar diagram illustrates the excitation probability. It is observed that the probability of higher excitation is very low. Therefore, we restrict analytical calculations to single excitations only, while the full Fock space is considered in numerical calculations. Under weak driving conditions, the ansatz quantum state of the system can be described as

$$|\psi\rangle = c_0|00g\rangle + c_1|10g\rangle + c_2|01g\rangle + c_3|00e\rangle, \tag{10}$$

where c_0, c_1, c_2, c_3 are complex amplitudes that satisfy the normalization condition:

$$|c_0|^2 + |c_1|^2 + |c_2|^2 + |c_3|^2 = 1. \tag{11}$$

The density matrix for the pure state is given by

$$\rho = |\psi\rangle\langle\psi|. \tag{12}$$

In the ordered basis $\{|00g\rangle, |10g\rangle, |01g\rangle, |00e\rangle\}$, the density matrix is a 4×4 outer product, but only the elements surviving the partial traces are needed for reduced density matrices. Under the weak-excitation approximation, the density matrix is defined in the single-excitation manifold. The entanglement measures are evaluated after appropriate partial tracing within this subspace. For entanglement quantification, concurrence is computed using the reduced two-subsystem density matrices obtained by tracing over the third subsystem within the truncated space. The reduced density matrix for subsystem i (e.g., resonator 1) is obtained via

$$(\rho_i)_{mn} = \sum_{y,z} \langle m, y, z|\rho|n, y, z\rangle, \quad m, n \in \{0, 1\}. \tag{13}$$

For subsystem 1, the matrix elements are

$$(\rho_1)_{00} = |c_0|^2 + |c_2|^2 + |c_3|^2, \tag{14}$$

$$(\rho_1)_{11} = |c_1|^2, \tag{15}$$

$$(\rho_1)_{01} = \sum_{y,z} \langle 0, y, z|\rho|1, y, z\rangle = c_0 c_1^*, \tag{16}$$

$$(\rho_1)_{10} = (\rho_1)_{01}^* = c_1 c_0^*. \tag{17}$$

Thus, the reduced density matrix for subsystem 1 is

$$\rho_1 = \begin{pmatrix} |c_0|^2 + |c_2|^2 + |c_3|^2 & c_0 c_1^* \\ c_1 c_0^* & |c_1|^2 \end{pmatrix}. \tag{18}$$

The determinant of ρ_1 is

$$\det \rho_1 = (|c_0|^2 + |c_2|^2 + |c_3|^2)|c_1|^2 - |c_0 c_1^*|^2 = |c_1|^2(|c_2|^2 + |c_3|^2). \tag{19}$$

The bipartite concurrence between subsystem i and the joint subsystem (jk) in a tripartite quantum system is defined as

$$\mathcal{C}_{i(jk)} = \sqrt{2(1 - \mathrm{Tr}_i[(\mathrm{Tr}_{jk}\,\rho)^2])}, \tag{20}$$

where $\mathrm{Tr}_{jk}\rho$ denotes the partial trace over subsystems j and k, yielding the reduced density matrix for subsystem i. The concurrence $\mathcal{C}_{i(jk)}$ quantifies the entanglement between subsystem i and the composite subsystem (jk), serving as an entanglement monotone that reflects the quantum correlations based on the purity of the reduced density matrix. Using the above, the concurrence for subsystem 1 is

$$\mathcal{C}_{1(23)} = 2|c_1|(\sqrt{|c_2|^2 + |c_3|^2}), \tag{21}$$

$$\mathcal{C}_{1(23)}^2 = 4|c_1|^2(|c_2|^2 + |c_3|^2). \tag{22}$$

Physically, $\mathcal{C}_{1(23)}$ measures the quantum correlation between resonator 1 and the combined subsystem of the atom and resonator 2. Note that a nonzero $\mathcal{C}_{1(23)}$ indicates that resonator 1 is entangled with the joint state of subsystems 2 and 3, implying that its quantum state cannot be described independently. If $\mathcal{C}_{1(23)} = 0$, resonator 1 is unentangled, and its state is separable from subsystems 2 and 3. Similarly,

$$\mathcal{C}_{2(31)} = 2|c_2|\sqrt{|c_3|^2 + |c_1|^2}, \tag{23}$$

$$\mathcal{C}_{3(12)} = 2|c_3|\sqrt{|c_1|^2 + |c_2|^2}. \tag{24}$$

These quantify the entanglement of subsystems 2 and 3 with their respective composite subsystems. Interestingly, we can also observe that the pairwise concurrences depend only on c_1, c_2 and c_3,

but not explicitly on the vacuum contribution. The vacuum state is fully separable and therefore does not contribute to entanglement generation. The entanglement measure, concurrence, quantifies only quantum correlations arising from excitation sharing and depends on coherence and population terms within the excited subspace.

To determine the coefficients c_n, we solve the Schrödinger equation $i\frac{d|\psi\rangle}{dt} = \hat{H}|\psi\rangle$ in the steady state using the effective Hamiltonian of Eq. (5). This yields the coupled equations

$$\left(\Delta - \frac{i\kappa}{2}\right)c_1 + Jc_2 + gc_3 + \Omega_1 c_0 = 0, \tag{25}$$

$$\left(\Delta - \frac{i\kappa}{2}\right)c_2 + Jc_1 + \Omega_2 c_0 = 0, \tag{26}$$

$$\left(\Delta_a - \frac{i\gamma}{2}\right)c_3 + gc_1 = 0. \tag{27}$$

After solving these equations, one can obtain the following solutions for the coefficients:

$$c_1 = \frac{\left(\Delta_a - \frac{i\gamma}{2}\right)\left(\Delta - \frac{i\kappa}{2}\right)\Omega_1 - \left(\Delta_a - \frac{i\gamma}{2}\right)J\Omega_2}{P}, \tag{28}$$

$$c_2 = \frac{\left(\Delta_a - \frac{i\gamma}{2}\right)\left(\Delta - \frac{i\kappa}{2}\right)\Omega_2 - \left(\Delta_a - \frac{i\gamma}{2}\right)J\Omega_1 - g^2\Omega_2}{P}, \tag{29}$$

$$c_3 = \frac{g\left[-\left(\Delta - \frac{i\kappa}{2}\right)\Omega_2 + J\Omega_1\right]}{P}, \tag{30}$$

where

$$P = \left(\Delta - \frac{i\kappa}{2}\right)^2\left(\Delta_a - \frac{i\gamma}{2}\right) - g^2\left(\Delta - \frac{i\kappa}{2}\right) - J^2\left(\Delta_a - \frac{i\gamma}{2}\right). \tag{31}$$

Substituting c_1, c_2, c_3 into the concurrence expressions yields $\mathcal{C}_{1(23)}, \mathcal{C}_{2(31)}, \mathcal{C}_{3(12)}$, enabling the calculation of the concurrence fill as defined in prior work [41].

At resonance, we require $P = 0$. Under critical coupling, the response of the coupled system is maximized. In this condition, the effective non-Hermitian matrix becomes singular, indicating enhanced excitation exchange and strong interference effects. This condition identifies the parameter regimes of maximal system response. Under resonance, the optimal atom-resonator coupling g will be

$$g = \sqrt{\frac{\Delta_a}{\Delta}\left(\Delta^2 - J^2 - \frac{\kappa^2}{4}\right) + \kappa\gamma}. \tag{32}$$

Similarly, the resonator-resonator coupling J can be expressed as

$$J = \sqrt{\frac{2g^2\Delta - \kappa\Delta\gamma}{\Delta_a} + \frac{\kappa^2}{4} - \Delta^2}. \tag{33}$$

Using the optimal coupling parameters g and J at resonance, we certify the tripartite entanglement measure, specifically the concurrence fill, in our resonator-atom-resonator model. The analytical results are derived using the effective Hamiltonian $\hat{H}_{\text{eff}}$. Analytically, we compute $\mathcal{C}_{1(23)}, \mathcal{C}_{2(31)}, \mathcal{C}_{3(12)}$ using the derived coefficients c_1, c_2, c_3 and evaluate the concurrence fill using eq. (8). Numerical results are obtained by solving the complete Lindblad master equation in Qutip to validate the analytical results. $\hat{H}_{\text{eff}}$ is used only for analytical derivations and to understand the physical picture of the excitation subspace. Here, trace preservation is ensured by the Lindblad formalism used in numerical calculations. Normalization is also properly enforced when extracting steady-state solutions from the effective model. A nonzero concurrence fill confirms genuine

tripartite entanglement, consistent with the geometric constraints of the concurrence triangle, ensuring robust certification across all bipartitions.

IV. RESULTS AND DISCUSSIONS

Initially, if we neglect the second cavity mode ($J = 0$ and $\Omega_2 = 0$), Eq. (2) reduces to the simplified Jaynes-Cummings model in the rotating reference frame. In this condition, we can treat the model as a single two-level atom interacting with a single quantized cavity mode. By using this assumption, the Hamiltonian can be rewritten as

$$\hat{H}_{\rm JC} = \Delta\hat{a}_1^\dagger\hat{a}_1 + \frac{\Delta_a}{2}\sigma_z + g(\hat{a}_1^\dagger\sigma_- + \hat{a}_1\sigma_+) + \Omega_1(\hat{a}_1^\dagger + \hat{a}_1). \tag{34}$$

Under this condition, the possible quantum state takes the form $|\psi\rangle = C_0|0g\rangle + C_1|0e\rangle + C_2|1g\rangle$. By substituting the ansatz state $|\psi\rangle$ into the Schrödinger equation $i\frac{d|\psi\rangle}{dt} = \hat{H}_{\rm JC}|\psi\rangle$, we evolve into a steady state and obtain the following equations:

$$\left(\Delta - \frac{i\kappa}{2}\right)C_1 + gC_2 + \Omega_1 C_0 = 0, \tag{35}$$

$$gC_1 + \left(\frac{\Delta_a}{2} - \frac{i\gamma}{2}\right)C_2 = 0. \tag{36}$$

After solving these two equations, we get the coefficient C_1, C_2 as

$$C_1 = \frac{\Omega_1\left(\frac{\Delta_a}{2} - \frac{i\gamma}{2}\right)}{D}, \quad C_2 = \frac{-\Omega_1 g}{D}, \tag{37}$$

where $D = (\Delta - \frac{i\kappa}{2})(\frac{\Delta_a}{2} - \frac{i\gamma}{2}) - g^2$. Under resonance conditions, the atom-resonator coupling strength will be

$$g = \sqrt{\left(\Delta - \frac{i\kappa}{2}\right)\left(\frac{\Delta_a}{2} - \frac{i\gamma}{2}\right)}. \tag{38}$$

We can calculate the atom-photon bipartite entanglement using concurrence ($\mathcal{C}$), which is a quantifier used to measure bipartite entanglement. One can write ($\mathcal{C}$) in terms of the probability amplitude coefficient as

$$\mathcal{C} = 2|C_2||C_1|. \tag{39}$$

Now, using the calculated values of C_1 and C_2 from Eq. (37), we analytically calculate the concurrence.

Figure 3 illustrates the variation of bipartite concurrence between the atom and the driven cavity mode under different coupling conditions. Figures 3(a) and 3(b) are plotted analytically from the analytical calculations, whereas Figs. 3(c) and 3(d) are plotted numerically by solving the full quantum master equation in Qutip [31] under the steady-state condition. To generate the analytical plot, we plug the values of the coefficients C_1 and C_2 in Eq. (37) into Eq. (39), and calculate the concurrence. For the plot, we have chosen experimentally feasible parameters as $\kappa = 1$, $\Delta_a = 1\kappa$, $\gamma = 0.1\kappa$, and $\Omega = 0.5\kappa$

As shown in Fig. 3(a), the concurrence exhibits a distinct resonance around $\frac{\Delta}{\kappa} \approx 0$, where the cavity and the atomic transitions are nearly resonant. This corresponds to the maximum hybridization between the atomic excitation $|e, 0\rangle$ and the single photon state $|g, 1\rangle$. The peak of the concurrence reflects the coherent exchange of excitation between the two subsystems.

The term $g(\hat{a}_1^\dagger\sigma_- + \hat{a}_1\sigma_+)$ couples the states $|e, 0\rangle \leftrightarrow |g, 1\rangle$ with coupling strength g. For a larger coupling strength $g = 0.6\kappa$, the splitting between dressed states increases, and the concurrence peak broadens due to enhanced atom-field mixing. For weak coupling $g = 0.3\kappa$, the hybridization is

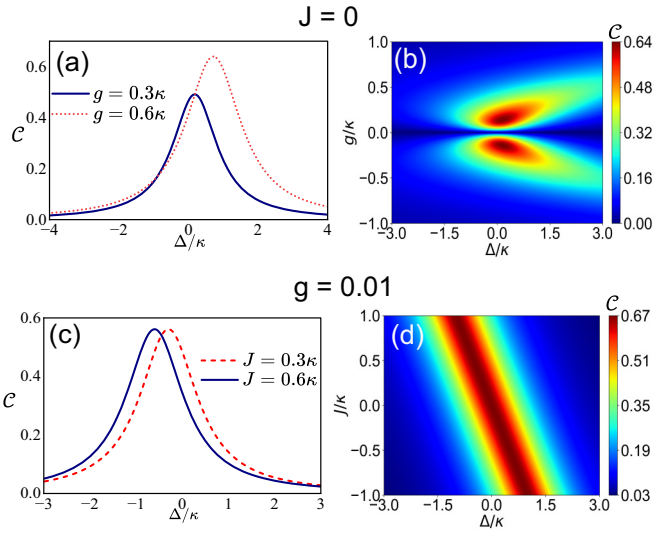


FIG. 3. Variation of bipartite concurrence with normalized detuning under different coupling regimes. (a) Steady-state concurrence as a function of normalized detuning for atom-resonator coupling strengths. (b) Surface plot of concurrence as a function of normalized detuning and coupling strength. (c) Concurrence as a function of normalized detuning for two photon-hopping strengths. (d) Surface plot of concurrence as a function of normalized detuning and coupling constant J.

reduced, resulting in a narrower and lower concurrence peak. These features clearly signify the role of the atom-resonator coupling in generating and controlling bipartite entanglement.

From Fig. 3(b), it can be observed that two bright lobes appear symmetrically about resonance, corresponding to the dressed-state splitting. The concurrence reaches its maximum when the energy exchange between the atom and the cavity is stronger. For large detuning, the interaction becomes off-resonant, which suppresses atom-photon coherence, and the concurrence is zero.

Figures 2(c) and 2(d) illustrate the bipartite concurrence when the photon-hopping interaction between the two resonators is occurring at very weak ($g = 0.001\kappa$) atom-resonator coupling. Under this condition, atom-field coupling becomes negligible, and the dominant correlation arises from photon delocalization between the two coupled cavities. Figure 2(c) suggests that the concurrence peak broadens as well as shifts slightly as J increases from 0.3κ to 0.6κ, as the normal modes of the coupled resonators hybridize. The corresponding surface plot in Fig. 2(d) confirms that the concurrence now scales mainly with $\frac{J}{\kappa}$, showing near-linear dependence in the weak-coupling limit. Physically, this indicates that entanglement is transferred from atom-cavity correlations to intercavity photonic correlations as the hopping interaction becomes dominant.

Next, we analyze the tripartite entanglement when both couplings are present (finite g and J). Initially, we consider the atom to be in the superposition state $\frac{1}{\sqrt{2}}(|0\rangle + |1\rangle)$, while both resonators are in the vacuum state $|0\rangle$. We use a conditional photon exchange interactions via the Jaynes-Cummings interaction to entangle the atom directly with the first resonator. Under the weak-excitation limit, only one excitation is present in the truncated Hilbert space. Through controlled time evolution, the excitation exchange occurs via coherent superposition, and multiexcitation states are excluded. After symmetric photon exchange by controlling each distinct photon excitation path with corresponding probabilities computed from the Schrödinger equation and interaction blocking (via quantum interference), the final state collapses to an entangled state. By applying symmetric, weak coupling between the atom and both resonators, we allow the single excitation to coherently distribute among all three subsystems. With precisely tuned coupling strengths and interaction times, destructive interference blocks multiexcitation pathways while constructive interference

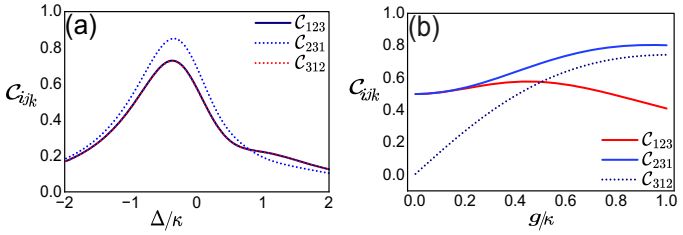


FIG. 4. (a) Variation of the bipartite concurrences as a function of normalized detuning in the hybrid regime where both the atom-cavity coupling and the intercavity hopping are finite. (b) Dependence of the three concurrences on the normalized atom-cavity coupling at fixed detuning.

amplifies the single-excitation symmetric state. The system evolves into a coherent superposition where exactly one of the three subsystems holds the excitation, forming a robust entangled state.

When both the atom-cavity coupling (g) and the intercavity hopping (J) are nonzero, the system enters a hybrid tripartite regime where atomic and photonic degrees of freedom are coherently mixed. Figure 4 illustrates the evolution of the three bipartite concurrences $\mathcal{C}_{1(23)}, \mathcal{C}_{2(31)}$, and $\mathcal{C}_{3(12)}$, which correspond to the sides of the concurrence triangle used to quantify the distribution of entanglement among the atom and the two resonators. We have analytically calculated $\mathcal{C}_{1(23)}, \mathcal{C}_{2(31)}$, and $\mathcal{C}_{3(12)}$ by plugging the coefficients of c_1, c_2, and c_3 from Eqs. (28)–(30) into Eqs. (20)–(23). Figure 2(a) illustrates the concurrence peaks near the resonance condition $\Delta \approx 0$, where the hybridized normal modes of the coupled system become degenerate and the excitation is maximally shared among the three subsystems. The near overlap of $\mathcal{C}_{1(23)}$ and $\mathcal{C}_{2(31)}$ arises from the structural symmetry between the two resonators, while the smaller magnitude of $\mathcal{C}_{3(12)}$ indicates that atomic participation is slightly suppressed due to spontaneous emission and detuning from the photonic resonance. Figure 4(b) shows the dependence of the concurrences on the normalized coupling strength. For weak coupling, the system remains predominantly photonic, and the entanglement is mainly confined between the two resonators via photon hopping J. As g increases, atom-photon coherence strengthens, leading to an enhanced redistribution of correlations among all three systems. In the strong-coupling regime, the three bipartite concurrences become comparable, signaling the formation of genuine tripartite hybrid entanglement where no single subsystem can be factorized from the others. This transition reflects the eventual balance between atom-mediated nonlinearity and photon-hopping coherence, establishing a steady-state hybridized field that is a coherent superposition of atomic and photonic excitations.

Figure 5 shows the behavior of the bipartite concurrence terms $\mathcal{C}_{1(23)}, \mathcal{C}_{2(31)}$, and $\mathcal{C}_{3(12)}$, which quantify how each subsystem (resonator 1, resonator 2, and the atom) is entangled with the

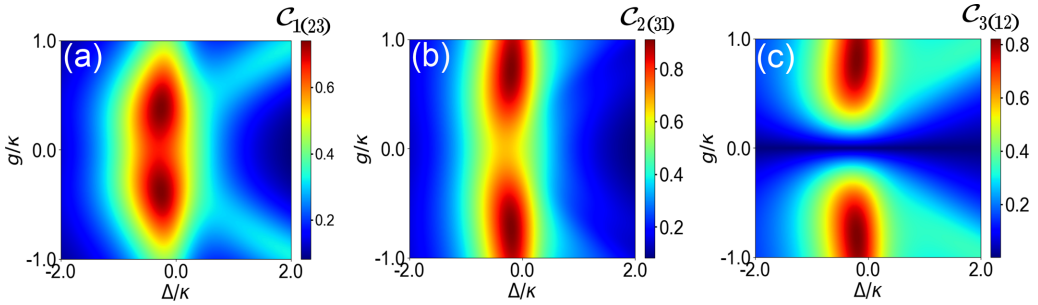


FIG. 5. Surface plots of bipartite concurrences as functions of normalized detuning and atom-cavity coupling strength g.

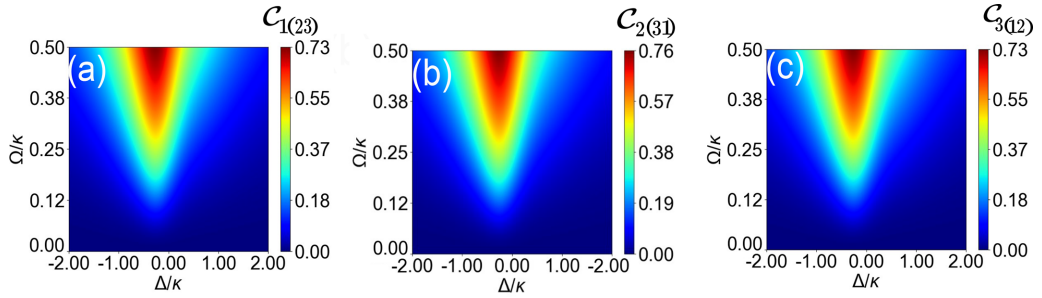


FIG. 6. Surface plots of bipartite concurrences as functions of normalized detuning and drive strength for nonzero atom-cavity (g) and intercavity (J) couplings. The bright regions mark the optimal drive, where coherent excitation exchange among the atom and both cavities generates maximal hybrid entanglement.

remaining two subsystems as a function of the normalized detuning and coupling strength. In Fig. 5(a), $\mathcal{C}_{1(23)}$ exhibits two distinct resonance lobes symmetrically placed around $\Delta = 0$, reflecting the hybridization between the first resonator and the collective atom-photon excitation manifold. This splitting corresponds to the well-known vacuum Rabi splitting in cavity QED, where the resonance condition is modified by the coupling strength g. As g increases, these lobes move apart, indicating stronger mixing between the photonic and atomic components in the normal-mode spectrum. Figure 5(b) $\mathcal{C}_{2(31)}$ displays a single pronounced vertical ridge near $\Delta = 0$. This suggests that the second resonator becomes maximally entangled with the atom-resonator-1 subsystem at resonance, where coherent photon exchange between the resonators (mediated by J) facilitates delocalization of the excitation across the network. In contrast, Fig. 5(c) $\mathcal{C}_{3(12)}$ shows a complementary structure, with the entanglement peaking for small-coupling strength and decreasing as g increases. Physically, this indicates that at weak coupling, the atom shares coherence with both resonators, but as g becomes large, the atom-resonator-1 subsystem becomes more isolated from resonator 2, reducing the atom's joint participation. All these plots reveal that the three bipartite concurrences are not independent but redistribute among the subsystems as the coupling strength and detuning are tuned.

From Fig. 6(a), it shows that as Ω increases from zero, the drive pumps photons into cavity 1, which couples both to the atom (through g) and to cavity 2 (through J). For small Ω, entanglement is weak because the field has insufficient amplitude to establish correlations between the subsystems. Around an optimal intermediate Ω (visible as the bright region at moderate $\frac{\Omega}{\kappa} \approx 0.4$–$0.6$), $\mathcal{C}_{1(23)}$ peak indicates maximum hybridization of the cavity 1 mode with both atom and cavity 2 [Fig. 6(b)]. Its profile is almost similar but slightly shifted because cavity 2 couples indirectly to the atom via photon hopping J. Increasing Ω enhances the photonic population transfer through J, producing strong photon-photon entanglement even slightly off resonance. The maximum again appears at moderate Ω, indicating optimal photon delocalization between the two cavities. Figure 6(c) illustrates that $\mathcal{C}_{3(12)}$ rises sharply with increasing Ω and saturates at high Ω, implying that the atomic excitation becomes strongly dressed by the photonic fields. The red region near zero detuning corresponds to the resonance condition where the dressed atomic-photonic state is maximally entangled. The bright regions mark the optimal drive, where coherent excitation exchange among the atom and both cavities generates maximal hybrid entanglement. We have used experimentally feasible parameters for the numerical plot, such as $\kappa = 1$, $\gamma = 0.1\kappa$, $\Delta_a = 1\kappa$, $\Omega = 0.5\kappa$, $J = 0.5\kappa$ (for fixed J), $g = 0.5\kappa$ (for fixed g).

Figure 7(a) illustrates the variation of concurrence fill ($\mathcal{F}_{123}$) with the atom-resonator coupling strength, with fixed inter-resonator coupling. The atom couples more strongly to cavity 1, enhancing the exchange of excitations between the atom and the photon field. This strong light-matter coupling leads to greater hybridization between atomic and photonic states, producing higher tripartite correlations that extend to cavity 2 via photon hopping. Consequently, the peak of $\mathcal{F}_{123}$ becomes

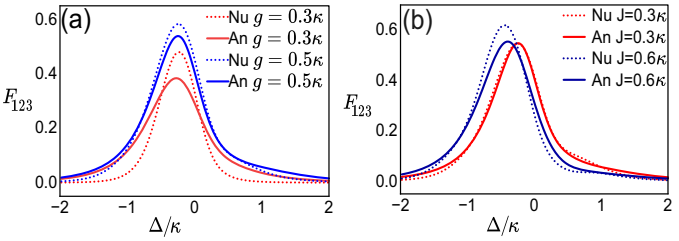


FIG. 7. Comparison of analytical (solid) and numerical (dotted) results for the tripartite entanglement measure, i.e., concurrence fill, as a function of normalized detuning. Here, "nu" and "an" stand for numerical and analytical results, respectively. (a) Variation with atom-cavity coupling g at fixed J. Stronger light-matter coupling enhances the hybridization between atomic and photonic excitations, yielding higher peak entanglement near resonance. (b) Variation with intercavity coupling J at fixed g. Increasing photon hopping broadens the resonance region and facilitates coherent excitation sharing across the full tripartite system.

higher and narrower near resonance, signifying a stronger and more coherent entanglement among the three subsystems. The enhancement with g arises because increasing the atom-photon coupling increases the dressed-state splitting and improves coherent excitation transfer, thereby generating entanglement across the entire hybrid system. Figure 7(b) shows the variation of $\mathcal{F}_{123}$ with the inter-resonator coupling strength for fixed atom-resonator coupling. The two resonators exchange photons via J, forming delocalized photonic modes. A moderate J allows the excitation initially coupled to the atom through cavity 1 to propagate coherently into cavity 2, thereby building up genuine tripartite entanglement. As J increases from 0.3κ to 0.6κ, the entanglement peak broadens slightly—indicating that stronger photon tunneling promotes energy-exchange coherence across the entire system, even slightly off resonance. The excellent agreement between numerical and analytical curves confirms the validity of the weak-drive analytical model. The driving strength controls the number of coherent excitations injected into the system. From Fig. 8(a), we can observe that for small Ω, the excitation probability is weak, so entanglement remains minimal. As Ω increases, the coherent population of the resonators enhances correlation between atomic and photonic degrees of freedom, resulting in a strong rise in $\mathcal{F}_{123}$. The V-shaped region centered at $\Delta \approx 0$ reflects the resonance condition where the driving field frequency matches the coupled system's dressed-state energies, maximizing coherent energy exchange. This indicates that the tripartite entanglement is drive assisted; the external field creates correlated excitations among the atom and both resonators most efficiently when driven near resonance. Figure 8(b) illustrates how increasing g enhances hybrid light-matter coupling, thereby amplifying the system's collective quantum correlations and enabling genuine tripartite entanglement. At $g \approx 0$, the system reduces to two weakly coupled photonic modes, giving almost zero $\mathcal{F}_{123}$. As g increases, energy hybridization between atomic and photonic excitations generates strong tripartite correlations, seen as the bright

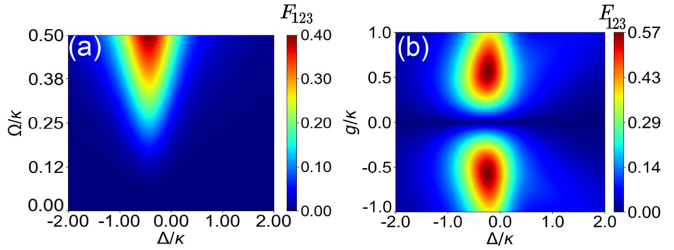


FIG. 8. Plots of the tripartite entanglement measure as functions of normalized detuning. (a) Dependence on driving strength, showing drive-induced enhancement of hybrid atom-photon correlations near resonance. (b) Dependence on atom-cavity coupling, where maximal entanglement occurs at resonance.

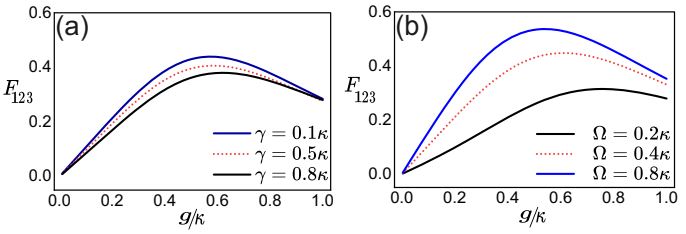


FIG. 9. Variation of tripartite entanglement with normalized atom-resonator coupling. (a) Dependence on the atomic decay rate shows suppression of hybrid correlations with increasing dissipation. (b) Dependence on driving strength with entanglement.

central region. The symmetric lobes around $\Delta = 0$ correspond to the upper and lower polaritonic branches of the Jaynes-Cummings ladder, where coherent superpositions of atom-photon states form. The entanglement is maximal at these hybridized resonances, where the atom effectively mediates nonclassical correlations between the two cavities.

Figure 9 illustrates how the tripartite entanglement measure $\mathcal{F}_{123}$ varies with the normalized atom-resonator coupling strength for different atomic decay rates (γ) and driving strengths (Ω), which provides a clear picture of how dissipation and external drive jointly influence multipartite hybrid entanglement in the system. Figure 9(a) shows as the coupling g increases from zero, the system transitions from a weak-coupling regime to a strong-coupling regime, enhancing coherent energy exchange between the atom and resonator 1. $\mathcal{F}_{123}$ increases initially, reaching a maximum at an optimal $\frac{g}{\kappa}$, and then decreases as excessive coupling splits the resonance and leads to reduced population overlap among the three modes. Increasing γ (atomic decay) suppresses the entanglement amplitude, since stronger spontaneous emission destroys atomic coherence and weakens atom-photon correlations. The observed peak reflects the balance between coherent atom-photon interaction and dissipative losses, characteristic of the photon-blockade-assisted hybrid entanglement regime. A small γ allows the atom to participate in collective hybridization, while a large γ rapidly projects the atom to its ground state, thereby washing out tripartite correlations. Figure 9(b) depicts the drive field acting as a tunable resource for injecting correlations into the coupled resonator-atom network. For fixed dissipation, increasing the external drive populates the resonators more efficiently, facilitating enhanced atom-photon and intercavity correlations, hence a rise in $\mathcal{F}_{123}$. The behavior shows a nonlinear response, with entanglement maximized under moderate coherent driving—strong enough to induce hybridization but weak enough to avoid saturation and decoherence.

V. CONCLUSION

In this work, we demonstrated that a hybrid resonator-atom-resonator system can serve as a practical and reconfigurable platform for generating multipartite quantum correlations in the steady state. By focusing on the weak-excitation regime, we derived an analytical steady-state description that captures how a single quantum of energy becomes coherently distributed among two photonic modes and an atom. Using bipartite concurrences together with the concurrence-fill measure, we identified clear regimes where these correlations combine to form robust tripartite entanglement, even in the presence of photon leakage and spontaneous emission. The strong agreement between our analytical predictions and full Lindblad-master-equation simulations confirms that the essential physics of hybrid steady-state entanglement can be understood and controlled using accessible system parameters.

Beyond establishing the feasibility of tripartite entanglement in this minimal hybrid node, our results offer direct guidance for implementing entanglement-assisted quantum networking. By tuning the atom-cavity coupling, photon-hopping strength, and coherent driving conditions, quantum information can be coherently routed and shared among multiple modes, enabling distributed

processing and communication within a scalable architecture. These insights position coupled cavity-QED systems as promising building blocks for future modular quantum networks that require stable, controllable, and persistent nonclassical correlations.

ACKNOWLEDGMENT

Prof. Shailendra K. Varshney acknowledge the support from National Quantum Mission (NQM), an initiative from the Department of Science & Technology (DST), Ministry of Education, New Delhi India.

DATA AVAILABILITY

The data can be obtained from the corresponding author upon reasonable request.

APPENDIX: COMPARATIVE STUDY OF TRIPARTITE ENTANGLEMENT QUANTIFIERS

For a quantum system composed of three subsystems, the monogamy property of bipartite entanglement quantified by concurrence was first described through the Coffman-Kundu-Wootters (CKW) inequality [42]. Later, CKW conjectured that this monogamy relation could be extended to systems containing multiple subsystems, which was subsequently proven by Osborne and Verstraete [43]. Furthermore, Gour *et al.* introduced a dual monogamy inequality for tripartite systems based on the concurrence of assistance (COA) [44,45]. Consider a tripartite quantum pure state $|\psi\rangle_{ABC}$ in a $2 \times 2 \times n$-dimensional Hilbert space shared by Alice, Bob, and Charlie. Charlie performs local measurements on subsystem C in order to maximize the entanglement between Alice and Bob. The reduced density matrix of subsystems A and B, obtained by tracing out Charlie's subsystem C, is

$$\rho_{AB} = \mathrm{Tr}_C(|\psi\rangle_{ABC}\langle\psi|). \tag{A1}$$

Let $\mathcal{E} = \{p_i, |\phi_i^{AB}\rangle\}$ be any decomposition of ρ_{AB} such that

$$\rho_{AB} = \sum_i p_i \left|\phi_i^{AB}\right\rangle\left\langle\phi_i^{AB}\right|, \sum_i p_i = 1. \tag{A2}$$

Then, the COA is defined as

$$C_a(|\psi\rangle_{ABC}) = \max_{\mathcal{E}} \sum_i p_i C\left(\left|\phi_i^{AB}\right\rangle\right). \tag{A3}$$

Similarly, for a given mixed state, the COA can be extended to mixed states in terms of convex roof construction as

$$C_a(\rho_{ABC}) = \min \sum_i p_i C_a(|\psi_i\rangle_{ABC}), \tag{A4}$$

where the minimum is taken over all decompositions $\{p_i, |\psi_i\rangle_{ABC}\}$ of ρ_{ABC}. For a $(2 \otimes 2 \otimes n)$-dimensional mixed state ρ_{ABC},

$$C_a^2(\rho_{ABC}) \geqslant C^2(\rho_{AB}) + \tau^2(\rho_{ABC}), \tag{A5}$$

where $\tau(\rho_{ABC})$ is the genuine tripartite entanglement measure for mixed states obtained by extending $\tau(\cdot)$ of pure states via the convex roof construction and $\rho_{AB} = \mathrm{tr}_C\, \rho_{ABC}$. If $\{p_k, |\psi^k\rangle_{ABC}\}$ is the optimal decomposition, then one can write

$$\tau(\rho_{ABC}) = \sum_k p_k \tau(|\psi^k\rangle_{ABC}) = \sum_k p_k \tau\left(\rho_{AB}^k\right), \tag{A6}$$

where

$$\rho_{AB}^k = \mathrm{tr}_C[|\psi^k\rangle_{ABC}\langle\psi^k|]. \tag{A7}$$

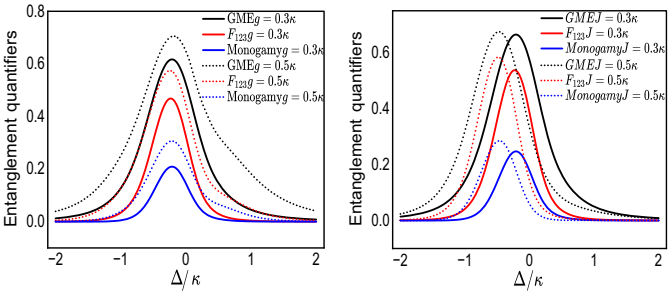


FIG. 10. Comparison of different tripartite entanglement quantifiers as a function of the normalized detuning $\frac{\Delta}{\kappa}$. GME concurrence, concurrence fill (F_{123}), and monogamy relations are shown for (a) two different atom-resonator coupling strengths $g = 0.3\kappa$ (solid lines) and $g = 0.5\kappa$ (dotted lines), and (b) two different inter-resonator coupling strengths $J = 0.3\kappa$ (solid lines) and $J = 0.5\kappa$ (dotted lines).

There is another quantifier genuine multipartite entanglement (GME) concurrence to quantify multipartite entanglement [46,47]. For n-partite pure states $|\Psi\rangle \in \mathcal{H}_1 \otimes \mathcal{H}_2 \otimes \cdots \otimes \mathcal{H}_n$, where $\dim(\mathcal{H}_i) = d_i$, $i = 1, 2, \ldots, n$, we can define the GME concurrence as [48]

$$C_{\mathrm{GME}}(|\Psi\rangle) := \min_{\gamma_i \in \gamma} \sqrt{2\big[1 - \mathrm{Tr}\big(\rho^2_{A_{\gamma_i}}\big)\big]}, \tag{A8}$$

where $\gamma = \{\gamma_i\}$ represents the set of all possible bipartitions $\{A_i|B_i\}$ of $\{1, 2, \ldots, n\}$. The GME concurrence can be generalized for mixed states ρ via a convex roof construction, i.e.,

$$C_{\mathrm{GME}}(\rho) = \inf_{\{p_i, |\psi_i\rangle\}} \sum_i p_i C_{\mathrm{GME}}(|\psi_i\rangle), \tag{A9}$$

where the infimum is taken over all possible decompositions $\rho = \sum_i p_i |\psi_i\rangle\langle\psi_i|$. For example, for a tripartite pure state $|\psi\rangle \in \mathcal{H}_1 \otimes \mathcal{H}_2 \otimes \mathcal{H}_3$, there are three possible bipartitions $\gamma = \{\{1|2, 3\}, \{2|1, 3\}, \{3|1, 2\}\}$. Consequently, the GME concurrence is

$$C_{\mathrm{GME}}(\psi) = \min\left\{\sqrt{2\big[1 - \mathrm{Tr}\big(\rho_1^2\big)\big]},\ \sqrt{2\big[1 - \mathrm{Tr}\big(\rho_2^2\big)\big]}, \sqrt{2\big[1 - \mathrm{Tr}\big(\rho_3^2\big)\big]}\right\}. \tag{A10}$$

The definition of $C_{\mathrm{GME}}(\rho)$ directly implies $C_{\mathrm{GME}}(\rho) > 0$ for all genuinely n-partite entangled states. Figures 10(a) and 10(b) depict the entanglement quantifiers, GME concurrence, concurrence fill, and monogamy relations as a function of the normalized detuning $\frac{\Delta}{\kappa}$ for (a) two different atom-resonator coupling strengths and (b) two different inter-resonator coupling strengths. It is observed that all three entanglement quantifiers exhibit remarkably similar qualitative behavior across the considered parameter regime, though all three quantifiers, mainly GME concurrence, concurrence fill, and monogamy relations, are constructed from different mathematical definitions. Each quantifier exhibits a peak in the vicinity of the resonance condition. This indicates the generation of strong tripartite quantum correlations when the coherent interactions between the coupled cavities and the atom are most effective. At resonance, the exchange of excitations between the subsystems is enhanced, and strong correlations build up between the three subsystems.

In the off-resonance situation, the excitation exchange between the three subsystems becomes inefficient, leading to the gradual disappearance of the shared correlations among the cavities and the atom. As the system moves away from resonance, all three measures gradually decrease and eventually approach zero. This reduction reflects the suppression of coherent interactions due to detuning and dissipation, weakening the system's ability to sustain tripartite quantum correlations.

Although the magnitudes of the quantifiers differ because of their distinct mathematical constructions, the overall trends remain consistent across all measures, confirming that they capture the same underlying physical phenomenon—the emergence of tripartite entanglement in the cavity-QED

system. This consistency indicates that the present model provides a useful platform for validating and comparing multipartite entanglement quantifiers within a realistically driven-dissipative quantum system, and it supports the reliability of these measures in characterizing correlation structures in open quantum systems.

[1] R. Horodecki, P. Horodecki, M. Horodecki, and K. Horodecki, Quantum entanglement, Rev. Mod. Phys. **81**, 865 (2009).

[2] V. Vedral, Quantum entanglement, Nat. Phys. **10**, 256 (2014).

[3] P. Bakhshinezhad, M. Mehboudi, C. R. I. Carceller, and A. Tavakoli, Scalable entanglement certification via quantum communication, PRX Quantum **5**, 020319 (2024).

[4] A. Datta and G. Vidal, Role of entanglement and correlations in mixed-state quantum computation, Phys. Rev. A **75**, 042310 (2007).

[5] S. Dooley, S. Pappalardi, and J. Goold, Entanglement enhanced metrology with quantum many-body scars, Phys. Rev. B **107**, 035123 (2023).

[6] W. Dür, G. Vidal, and J. I. Cirac, Three qubits can be entangled in two inequivalent ways, Phys. Rev. A **62**, 062314 (2000).

[7] M. Erhard, M. Krenn, and A. Zeilinger, Advances in high-dimensional quantum entanglement, Nat. Rev. Phys. **2**, 365 (2020).

[8] A. M. Lance, T. Symul, W. P. Bowen, B. C. Sanders, and P. K. Lam, Tripartite quantum state sharing, Phys. Rev. Lett. **92**, 177903 (2004).

[9] S. Y. Looi and R. B. Griffiths, Tripartite entanglement in qudit stabilizer states and application in quantum error correction, Phys. Rev. A **84**, 052306 (2011).

[10] X. Ge, L. Liu, and S. Cheng, Tripartite entanglement measure under local operations and classical communication, Phys. Rev. A **107**, 032405 (2023).

[11] T. J. Elliott, W. Kozlowski, S. F. Caballero-Benitez, and I. B. Mekhov, Multipartite entangled spatial modes of ultracold atoms generated and controlled by quantum measurement, Phys. Rev. Lett. **114**, 113604 (2015).

[12] G. Mathew, S. L. L. Silva, A. Jain, A. Mohan, D. T. Adroja, V. G. Sakai, C. V. Tomy, A. Banerjee, R. Goreti, V. N. Aswathi, R. Singh, and D. Jaiswal-Nagar, Experimental realization of multipartite entanglement via quantum Fisher information in a uniform antiferromagnetic quantum spin chain, Phys. Rev. Res. **2**, 043329 (2020).

[13] F. Shi, L. Chen, G. Chiribella, and Q. Zhao, Entanglement detection length of multipartite quantum states, Phys. Rev. Lett. **134**, 050201 (2025).

[14] D. A. Meyer and N. Wallach, Global entanglement in multiparticle systems, J. Math. Phys. **43**, 4273 (2002).

[15] T.-C. Wei and P. M. Goldbart, Geometric measure of entanglement and applications to bipartite and multipartite quantum states, Phys. Rev. A **68**, 042307 (2003).

[16] A. Osterloh and J. Siewert, Constructing n-qubit entanglement monotones from antilinear operators, Phys. Rev. A **72**, 012337 (2005).

[17] Y. Li and J. Shang, Geometric mean of bipartite concurrences as a genuine multipartite entanglement measure, Phys. Rev. Res. **4**, 023059 (2022).

[18] G. Burkard, M. J. Gullans, X. Mi, and J. R. Petta, Superconductor–semiconductor hybrid-circuit quantum electrodynamics, Nat. Rev. Phys. **2**, 129 (2020).

[19] D. De Bernardis, T. Jaako, and P. Rabl, Cavity quantum electrodynamics in the nonperturbative regime, Phys. Rev. A **97**, 043820 (2018).

[20] I. M. Georgescu, S. Ashhab, and F. Nori, Quantum simulation, Rev. Mod. Phys. **86**, 153 (2014).

[21] A. Stockklauser, P. Scarlino, J. V. Koski, S. Gasparinetti, C. K. Andersen, C. Reichl, W. Wegscheider, T. Ihn, K. Ensslin, and A. Wallraff, Strong coupling cavity QED with gate-defined double quantum dots enabled by a high impedance resonator, Phys. Rev. X **7**, 011030 (2017).

[22] Y.-F. Xiao, Y.-C. Liu, B.-B. Li, Y.-L. Chen, Y. Li, and Q. Gong, Strongly enhanced light-matter interaction in a hybrid photonic-plasmonic resonator, Phys. Rev. A **85**, 031805 (2012).

[23] F. Casagrande, A. Lulli, and M. G. A. Paris, Tripartite entanglement transfer from flying modes to localized qubits, Phys. Rev. A **79**, 022307 (2009).
[24] Y. Zhang, T. Liu, J. Zhao, Y. Yu, and C.-P. Yang, Generation of hybrid Greenberger-Horne-Zeilinger entangled states of particlelike and wavelike optical qubits in circuit QED, Phys. Rev. A **101**, 062334 (2020).
[25] R. Rogers, N. Cummings, L. M. Pedrotti, and P. Rice, Atom-field entanglement in cavity QED: Nonlinearity and saturation, Phys. Rev. A **96**, 052311 (2017).
[26] H. Flayac, D. Gerace, and V. Savona, An all-silicon single-photon source by unconventional photon blockade, Sci. Rep. **5**, 11223 (2015).
[27] E. Z. Casalengua, J. C. L. Carreño, F. P. Laussy, and E. del Valle, Conventional and unconventional photon statistics, Laser Photon. Rev. **14**, 1900279 (2020).
[28] K. J. Vahala, Optical microcavities, Nature **424**, 839 (2003).
[29] S. M. Spillane, T. J. Kippenberg, O. J. Painter, and K. J. Vahala, Ideality in a fiber-taper-coupled microresonator system for application to cavity quantum electrodynamics, Phys. Rev. Lett. **91**, 043902 (2003).
[30] P. Forn-Díaz, L. Lamata, E. Rico, J. Kono, and E. Solano, Ultrastrong coupling regimes of light-matter interaction, Rev. Mod. Phys. **91**, 025005 (2019).
[31] J. R. Johansson, P. D. Nation, and F. Nori, QuTiP: An open-source Python framework for the dynamics of open quantum systems, Comput. Phys. Commun. **183**, 1760 (2012).
[32] C. H. Bennett, D. P. DiVincenzo, J. A. Smolin, and W. K. Wootters, Mixed-state entanglement and quantum error correction, Phys. Rev. A **54**, 3824 (1996).
[33] W. K. Wootters, Entanglement of formation of an arbitrary state of two qubits, Phys. Rev. Lett. **80**, 2245 (1998).
[34] C. H. Bennett, H. J. Bernstein, S. Popescu, and B. Schumacher, Concentrating partial entanglement by local operations, Phys. Rev. A **53**, 2046 (1996).
[35] G. Vidal and R. F. Werner, Computable measure of entanglement, Phys. Rev. A **65**, 032314 (2002).
[36] M. Horodecki, P. Horodecki, and R. Horodecki, Separability of mixed states: Necessary and sufficient conditions, Phys. Lett. A **223**, 1 (1996).
[37] A. Peres, Separability criterion for density matrices, Phys. Rev. Lett. **77**, 1413 (1996).
[38] M. A. Nielsen and I. L. Chuang, *Quantum Computation and Quantum Information* (Cambridge University Press, Cambridge, UK, 2010), 10th anniversary ed.
[39] C. Eltschka and J. Siewert, Monogamy equalities for qubit entanglement from Lorentz invariance, Phys. Rev. Lett. **114**, 140402 (2015).
[40] S. Xie and J. H. Eberly, Triangle measure of tripartite entanglement, Phys. Rev. Lett. **127**, 040403 (2021).
[41] Z.-X. Jin, Y.-H. Tao, Y.-T. Gui, S.-M. Fei, X. Li-Jost, and C.-F. Qiao, Concurrence triangle induced genuine multipartite entanglement measure, Results Phys. **44**, 106155 (2023).
[42] V. Coffman, J. Kundu, and W. K. Wootters, Distributed entanglement, Phys. Rev. A **61**, 052306 (2000).
[43] T. J. Osborne and F. Verstraete, General monogamy inequality for bipartite qubit entanglement, Phys. Rev. Lett. **96**, 220503 (2006).
[44] G. Gour, Mixed-state entanglement of assistance and the generalized concurrence, Phys. Rev. A **72**, 042318 (2005).
[45] G. Gour, D. A. Meyer, and B. C. Sanders, Deterministic entanglement of assistance and monogamy constraints, Phys. Rev. A **72**, 042329 (2005).
[46] S. M. H. Rafsanjani, M. Huber, C. J. Broadbent, and J. H. Eberly, Genuinely multipartite concurrence of N-qubit X matrices, Phys. Rev. A **86**, 062303 (2012).
[47] D.-D. Dong, L.-J. Li, X.-K. Song, L. Ye, and D. Wang, Quantifying genuine tripartite entanglement by reshaping the state, Phys. Rev. A **110**, 032420 (2024).
[48] Z.-H. Ma, Z.-H. Chen, J.-L. Chen, C. Spengler, A. Gabriel, and M. Huber, Measure of genuine multipartite entanglement with computable lower bounds, Phys. Rev. A **83**, 062325 (2011).